Short Communication

Assessing the potential of Eddy detection in MIZ using SAR and Lagrangian modeling: A test case on Fram Strait

Nikita Sandalyuk [a,‡], Eduard Khachatrian [b,*,‡], Maxim Budyansky [c]

[a] Laboratory of Arctic Oceanography, The Moscow Institute of Physics and Technology, 9 Institutskiy per., Dolgoprudny, Moscow 141701, Russia
[b] Department of Physics and Technology, UiT The Arctic University of Norway, NO-9037 Tromsø, Norway
[c] V.I.Il'ichev Pacific Oceanological Institute, 3 Baltiyskaya St., Vladivostok 690041, Russia

A B S T R A C T

The analysis of ocean eddies in the marginal ice zone via remote sensing and modeling data is a challenging task. However, it is of crucial importance for various scientific applications and anthropogenic activities in the Arctic. Models often struggle to accurately represent eddies near the MIZ due to the intricate nature of sea ice-ocean interactions, unresolved small-scale processes, and coarse resolution. Nevertheless, combining the information provided from both SAR and model data offers promising results that can potentially improve eddy detection accuracy near the MIZ. Furthermore, accurate characterization of the spatial and temporal variability of eddies near the MIZ demands a holistic approach that incorporates multi-platform observations, including numerical models and remote sensing data. This study demonstrates a specific test case on the intercomparison of the eddy signatures located in the MIZ in the Fram Strait based on remote sensing SAR scenes and Lagrangian modeling data from the two global oceanographic reanalysis GOFS 3.1 and GLORYS 12 V1. The study specifically displays the strong agreement in the eddy polarity and synchronism with reality, as well as differences in spatial scales and location of eddy centers. Overall, the obtained results support the further use of the presented approach for studying the eddies in the MIZ regions in the Arctic.

1. Introduction

A marginal ice zone (MIZ) is a transitional region between the open ocean and dense sea ice, which is characterized by highly intense dynamics, exchanges of energy and heat between ocean, sea ice, and atmosphere, strong lateral buoyancy gradients, and enhanced primary production (Kozlov et al., 2020; Johannessen et al., 1987). Arctic MIZ is generally defined as the region with the sea ice concentration (SIC) between 15 and 80% and composed of different ice types (mostly brash ice) (WMO, 1970). Brash ice serves as a good tracer of dynamical processes in the MIZ and allows the identification of the geometrical structures of surface eddy signatures. However, visual interpretation of the eddy signatures based on the sea ice presents certain challenges and should be approached with caution.

Eddy formation is a typical dynamic process in the MIZ. The eddies are responsible for the trapping and transferring of trillions of tons of water (Jayne and Marotzke, 2002), which in turn plays a crucial role in mass, heat, and momentum exchange, affecting the location of the ice edge and enhancing the biological productivity processes (Johannessen et al., 1987; von Appen et al., 2018). Therefore, information about the eddy dynamics in the MIZ is of key importance for ocean and climate modeling in polar regions, as well as for fisheries in polar seas. A characteristic surface manifestation of an eddy in the MIZ region is a closed spiral-like circular pattern, with either cyclonic or anticyclonic rotational direction. Due to the sophisticated dynamic, other eddy patterns can appear on the ocean surface, such as vortex pairs or eddy dipoles and mushroom-like patterns, formed with both cyclonic and anticyclonic eddies.

The primary source of information about ocean mesoscale variability is satellite altimetry. The crucial benefit of such sensors is the ability to provide comprehensive coverage over the World's Ocean areas, which allowed oceanographers to collect a global altimetry time series for the last three decades (Chelton et al., 2011; Mason et al., 2014; Faghmous et al., 2015; Pegliasco et al., 2022). Moreover, the gridded altimetry products acquired by merging data from multiple missions provide a significant amount of statistical information about eddy characteristics,

---

such as the number of generated eddies, translation velocities, their geometric structure, and physical properties that can be used for further development and implementation of various automated eddy detection algorithms (Chelton et al., 2011; Mason et al., 2014; Faghmous et al., 2015). Nevertheless, the altimetry data have substantial limitations for eddy detection in the polar areas due to the presence of sea ice. Moreover, the gridded altimetry fields from AVISO (Archiving, Validation and Interpretation of Satellite Oceanographic data) resolve only a small number of eddies in the polar regions with a typical radius of 30–50 km, while Arctic eddies are several times smaller in diameter than low-latitude eddies due to significantly smaller Rossby radius of deformation compared with the mid-latitude oceans. It should be also mentioned that Rossby radius of deformation is much smaller on the Arctic shelf due to shallow depth. Therefore, information about eddies with spatial scales under 30 km is heavily overlooked (Bashmachnikov et al., 2020). Eventually, altimetry data is essentially unemployed for eddy detection near the MIZ.

Nowadays, the most versatile though not commonly used source of information on eddy dynamics in polar regions is satellite data from synthetic aperture radar (SAR) (Kozlov et al., 2020; Kozlov et al., 2019a; Kozlov and Atadzhanova, 2022). SAR operates at different characteristics, such as frequency bands, polarization channels, and spatial resolutions. It responds to dielectric properties, geometry, and roughness, as well as to an object's surface structure and – if the radiation penetrates the object – to its volume structure. The crucial advantage of this sensor is complete independence of solar illumination and weather conditions, due to the wavelengths that are perfectly able to penetrate through dense clouds (Sandven et al., 1993). This is a key point since dense cloud cover and lengthy periods of darkness are predominant in the polar regions for several months during the polar winter. The aforementioned features of the SAR are combined with a high spatial resolution capable of resolving ocean dynamics at the scales of 0.1–1 km. The above-mentioned advantages make the SAR sensor the most suitable instrument for monitoring eddy dynamics in the MIZ regions.

The region of interest (ROI) of this study is located over the Fram Strait (see Fig. 1). It is a 600 km wide passage between the Svalbard archipelago and Greenland that is the only deep passage from the Nordic Seas to the Arctic Ocean with a maximum depth of around 2600 m (von Appen et al., 2015). The Fram Strait represents an important and unique deep-water connection between the Arctic Ocean and the rest of the

World Ocean. The two primary currents that control the water mass exchange in that area are the West Spitsbergen Current (WSC) and the East Greenland Current (EGC). Eventually, Fram Strait is an unsurpassed place to study eddies in the MIZ due to the combination of several factors. First and foremost it is one of the most dynamically active regions in the Northern Atlantic from the ocean circulation point of view. Furthermore, it is the main gateway for sea ice to leave the Arctic Ocean. In (Kozlov and Atadzhanova, 2022) authors refer to the ROI as the Fram Eddy Band (75–80°N) which includes several hotspots with the highest probability of eddy generation. One of such hotspots is considered in our work for a more detailed study of eddy generation patterns and comparison with the model data.

Mesoscale and submesoscale eddies in the Fram Strait have previously been investigated in several studies (Kozlov et al., 2020; Bashmachnikov et al., 2020; Kozlov et al., 2019a; Kozlov and Atadzhanova, 2022; Kozlov et al., 2019b; Wekerle et al., 2020). For most works the primary source of information about the eddy physical and kinematic characteristics in this region are different types of satellite data and only SAR data were used to study MIZ eddies.

Eddy-resolving models represent an important source of data on the eddy dynamics in the polar regions. However, to properly resolve an eddies in the MIZ high spatial resolution is needed which in turn leads to the high computational cost of such simulations. Moreover, sparse in situ measurements, the presence of sea ice, and a poor understanding of the mechanisms of the eddy generation in the MIZ introduce large uncertainties to the ocean modeling in the MIZ. Several studies describe the capabilities of the high-resolution ocean–sea ice models such as FESOM and ROMS to resolve mesoscale and submesoscale structures in the Fram Strait region (Bashmachnikov et al., 2020; Wekerle et al., 2020; Wang et al., 2020). The simulation results are compared either with data from various satellite sensors (Bashmachnikov et al., 2020) or with simulation from another model (Wekerle et al., 2020). It should be also noted that in both studies authors either avoid the detection of the eddies in the MIZ (Bashmachnikov et al., 2020) or choose the specific depth level for eddy detection (Wekerle et al., 2020) and mostly focus on the inter-comparison of eddy census statistics, in particular, their physical and geometrical properties. However, there are no studies on the evaluation of the numerical model simulations of eddy dynamics in the high eddy active MIZ in the Fram Strait, as well as for the whole Arctic Region. Such research will help to increase our understanding of eddy dynamics
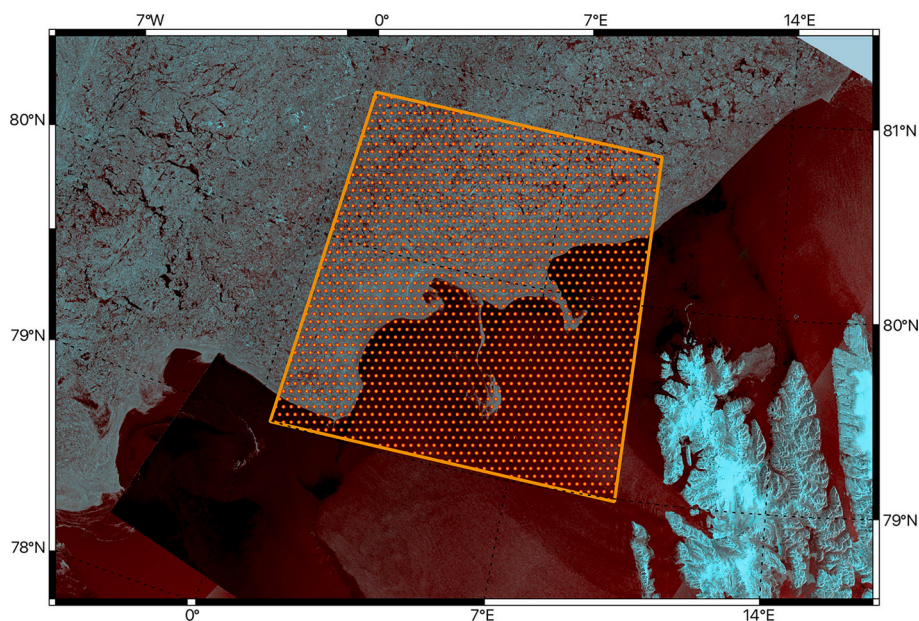
Fig. 1. Study area over the Fram Strait. False-color composite representations of SAR images (HH, HV, and HV as RGB) illustrate the total coverage of all the images used in this study. The orange rectangle represents the ROI that demonstrates the location of all eddies used in this study.

in the MIZ region and create a reference for developing parameterizations required by high-resolution ocean models.

Lagrangian approach with the current velocity fields as input data is a common tool for studying ocean circulation. The most commonly employed source of velocity currents utilized in Lagrangian methodology is AVISO satellite altimetry data fields which provide a reliable representation of the large-scale circulation in the surface layer of the World Ocean. However, satellite altimetry data do not provide information on the circulation in the underlying layers. Moreover, the velocities from altimetry fields are calculated using the geostrophic balance equation. It is well known that the geostrophic balance is predominant in the open ocean but in the coastal zones, the influence of nonlinear terms of the equations of motion are prevailing. The utilization of altimetry data for the calculation of currents in the coastal zones requires a complex sequence of processing steps, such as an implementation of waveform retracking algorithms (Roscher et al., 2017; Wang and Ichikawa, 2017). Hence, the altimetry data cannot be used to directly calculate currents in the coastal areas. The use of mathematical ocean modeling can solve this problem but the tuning of a high-resolution ocean model to a specific region is a very time-consuming and resource-intensive process. The only alternative is using the oceanographic reanalyses.

In the presented case study as input data for Lagrangian modeling we use velocity fields in the surface layer obtained from the GOFS 3.1 (Wallcraft et al., 2009) and GLORYS 12 V1 (Jean-Michel et al., 2021) oceanographic reanalyses, which are based on two different models that use different numerical schemes and approaches to simulate the physical ocean processes. Both models use different bathymetry, horizontal resolution, initial condition fields, sea ice modeling approaches, and more.

The key goal of this study is to compare the recognition and evolution of the eddies identified from SAR observations with the complementary fields obtained from the Lagrangian modeling based on a test case eddy structure from Fram Strait. The corresponding eddy structure was visually recognizable in the MIZ for more than a week providing us a unique opportunity to perform a distinct visual examination. We additionally aim to demonstrate the complementarity of each of the data sources as well as their differences and similarities. Accordingly, we provide a detailed analysis of eddies identified from different sources and describe their structural and geometric variability. It is worth mentioning that the sources used in this test case were not previously compared mutually. We are trying to provide evidence that the model data can be used in the MIZ for eddy detection.

2. Datasets and methods

The following section describes the datasets and methods used in this study. The region of interest for this study, i.e. Fram Strait, was carefully selected based on its high relevance to the research objectives and its potential to provide valuable insights into the investigation of eddy detection in the MIZ.

2.1. Datasets

In the presented study, we use the data from the two data sets: the Global Ocean Forecasting System (GOFS 3.1) reanalysis, which is built on HYCOM model (Wallcraft et al., 2009), and Copernicus Global 1/12° Oceanic and Sea Ice Reanalysis (GLORYS 12 V1) (Jean-Michel et al., 2021). The GLORYS 12 V1 is based on a global ocean general circulation model NEMO (Nucleus for European Modeling of the Ocean) (Madec, 2008). The two different numerical schemes are implemented in the models. In the abovementioned reanalyses, different sets of in-situ data and assimilation methods are used. The most important differences that can lead to not only quantitative but also qualitative differences in modeling results are the following. Both models use different types of vertical coordinates – a hybrid one for HYCOM and a combination of s- and z-coordinates for NEMO, as well as different sources of atmospheric

data and different data assimilation models. The GLORYS 12 V1 was also assessed against hydrographic observations obtained in the North Atlantic (Verezemskaya et al., 2021). It has been shown that reanalyses reproduce the major mesoscale eddy features and provide the large-scale context of their location (Verezemskaya et al., 2021). The GOFS 3.1 has also been exploited for the investigation of various eddy properties and eddy-current interaction (Ma et al., 2021; Zhang et al., 2021; Shinoda et al., 2023). However, both reanalyses have not yet been validated in the MIZ. Currently, there are no studies that investigate and evaluate eddy dynamics in the MIZ based on these datasets.

2.1.1. Remote sensing data

The Sentinel-1 images were acquired in extra-wide (EW) swath mode in dual polarization (HH and HV) at 40 m spatial resolution. Sentinel-1 operates at the C-band (central frequency of 5.404 GHz) and includes two polar-orbit Sentinel-1 A and Sentinel-1B missions that provide multiple sensing modes, such as stripmap, wave, interferometric wide, and extra-wide swath. The choice of sensing mode strongly relies on scientific goals, application, and availability of corresponding images. EW mode is primarily used for coastal observations including oil spill and sea-ice monitoring due to the ability to acquire data over a wide area of over 400 km.

Sentinel-1 data are publicly available through Copernicus Open Access Hub (European Union's Earth observation programme). The dataset was acquired for the Fram Strait region for the period of 5 days in the first two weeks of January 2023. Additionally, Sentinel-1 scenes used in this study were corrected for thermal noise and calibrated to sigma-nought in dB using the ESA Sentinel-1 Toolbox.

2.1.2. Lagrangian methodology

Velocity fields in the Lagrangian approach are considered on the grid domain as discrete data sets and used to track particle trajectories. For this purpose, the advection equations are solved for passive particles in a given velocity field.

$$\frac{d\lambda}{dt} = u(\lambda, \varphi, t), \tag{1}$$

$$\frac{d\varphi}{dt} = v(\lambda, \varphi, t), \tag{2}$$

where φ and λ are latitude and longitude, u and v are angular zonal and meridional velocities, respectively. The trajectories are computed by integrating eqs. (1-2) by using the method described in (Budyansky et al., 2022). For each passive particle, the length of its trajectory

$$S = R_E \int_{t_1}^{t_2} \sqrt{u^2(t)cos^2\varphi(t) + v^2(t)}dt \tag{3}$$

is calculated for 15 days in this study, where $R_E = 6371$ km. It is just the length of the curve traced by a trajectory of the advected particle from its initial position to the final one (Prants et al., 2017). Accordingly, we will refer to it as S-value, i.e. the length of the passive marker's trajectory on the spheroid over a 15-day period. Additionally, we use the term S-maps which simply visualizes the S-value in kilometers for a specific region of interest.

The surface velocity fields from the GOFS3.1 and GLORYS 12 V1 reanalysis were used for Lagrangian modeling. For each day during the time period from December 15, 2022 to January 15, 2023, the study area was filled with markers with initial coordinates on a uniform 500 × 500 grid. The calculation time of each trajectory for each marker is 15 days in reverse.

Eddy structures in the Lagrangian approach are represented as moving bodies of water or other substances that evolve during their propagation in the ocean. Eddy centers are elliptical points (stable stationary points of the two-dimensional velocity field). The regions of instability at the eddy boundary are associated with hyperbolic points

(unstable stationary points of the two-dimensional velocity field) (Prants et al., 2017; Prants et al., 2015; Prants et al., 2023).

Within the Lagrangian approach, each elementary volume of water can be associated with certain physicochemical properties (temperature, salinity, density, radioactivity, etc.). The chosen property serves as an indicator of the propagating water particle. Moreover, the trajectory function which carries key dynamic information can be assigned to each water particle. This approach allows us to obtain a detailed visualization of the eddy water exchange process, as well as various stages of eddy formation, splitting, merging, and dissipation.

Lyapunov maps (L-maps) offer additional insights into the observed eddy structures. For each point of the map, the largest singular number of the evolution matrix of the linearized system of eqs. (1 and 2) is

calculated. The logarithm of this number is divided by the integration period (15 days in our study). Detailed description of the calculation of the Lyapunov exponent is given in work (Prants et al., 2015).

3. Experimental results

This section presents a comparison of Sentinel-1 SAR scenes in MIZ and corresponding Lagrangian S-maps constructed by the method of Lagrangian modeling. Lagrangian maps proved to be a useful tool for studying mesoscale eddy structures (Prants et al., 2011; Prants et al., 2013; Prants et al., 2016; Travkin et al., 2022). The color coding on the S-maps indicates the distance traveled by the Lagrangian particles 15 days before the date of observation. The period of 01–10 January 2023 is
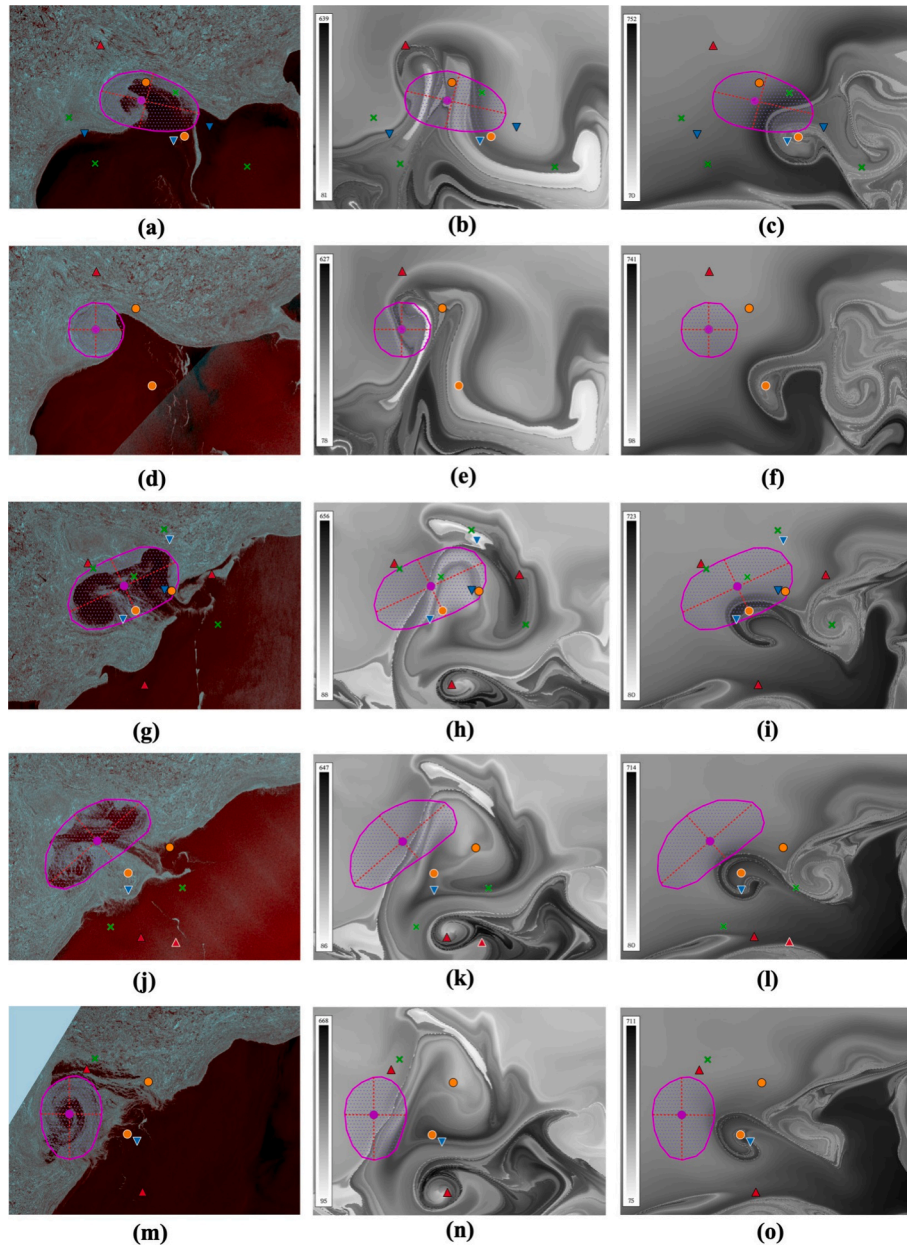
Fig. 2. False-color composite representations of Sentinel-1 SAR images (first column), S-maps from the GLORYS 12 V1 (second column), and GOFS 3.1 (third column) for 03 (a–c), 04 (d–f), 08 (g–i), 09 (j–l), and 10 (m–o) of January 2023. The purple polygon demonstrates the approximate boundary of the corresponding eddy signature manually detected from the SAR scene while the purple circle illustrates its center. Orange circles display the eddy center for GLORYS 12 V1 (orange circle with black boundary) and GOFS 3.1 (orange circle with white boundary). The upward-oriented (red) and downward-oriented (blue) triangles are elliptic points corresponding to locations of the centers of anticyclones and cyclones, and green crosses are locations of hyperbolic points (black symbol boundary refers to GLORYS 12 V1, while white boundary corresponds to GOFS 3.1). The values of S are in kilometers. (For interpretation of the references to color in this figure legend, the reader is referred to the web version of this article.)

selected for several reasons. During these dates, the ROI was homogeneously covered with several SAR scenes. In presented cases, we can identify the same eddy repeatedly on two consequent SAR images (with a 1-day interval in between). Moreover, the middle of winter is the period of the highest intensity of eddy generation in the MIZ over the Fram Strait (Kozlov and Atadzhanova, 2022). Here we consider SAR data as ground truth information on the dynamic processes in the ROI. The next few paragraphs describe several cases, aiming to find links between eddies detected in SAR and model data.

Based on a visual examination we identified the cyclonic eddy structures on the SAR images. The corresponding S-maps from both GLORYS 12 V1 and GOFS 3.1 show similar eddy-shaped signatures with the same polarity (Fig. 2). Moreover, according to the information provided by the consequent SAR scenes, we can conclude that the images represent different development stages of a single eddy. Both the model and satellite scenes provide the same result regarding the rotational direction of the eddies. Table 1 displays several important characteristics of manually detected individual eddies for both SAR and model data. There is a significant displacement between the eddy centers identified from the SAR and model. For the collocated eddy pairs the average displacement is 27 km and 25 km for the SAR-GLORYS 12 V1 and SAR-GOFS 3.1 respectively. However, on the date 03.01 eddy center from GLORYS 12 V1 is very close (8 km) to the respective eddy center from SAR.

The approximate eddy boundary on the S-maps can be defined as a closed eddy-shaped curve with the maximal gradient of the S value which differentiates waters engaged in the rotational motion around the eddy center from ambient waters. In the eddy centers the S-value reaches about 320 km and 490 km from the GLORYS 12 V1 and GOFS 3.1 respectively. On the eddy edges the S-values can reach 480 km for GLORYS 12 V1 and 660 km for the GOFS 3.1 which means that the velocities in central and peripheral parts of the eddies differ by >30%.

The eddy edge on the SAR image is identified as the outermost closed contour revealed by the sea ice which serves as the main tracer of the dynamical processes in the MIZ. The eddy spatial scales retrieved from SAR scenes are, on average, 1.5 times less than those in GLORYS 12 V1. The eddy spatial scales from the GOFS 3.1 date are closer to SAR and exceed those of about 0.5 times. The assessments of eddy scales from all three sources significantly exceed the estimation of Rossby baroclinic deformation radius for the ROI (4–6 km) (von Appen et al., 2016). It should also be noted that the definition of the eddy borders based on the visual examination of SAR scenes as well as the S-maps gives us a very rough estimation of eddy spatial scales.

L-maps (Fig. 3) provide a visual representation of Lagrangian coherence and help to identify more clearly the boundaries of mesoscale eddies, as well as their coherence and strength. The Lyapunov exponent quantitatively determines the rate of divergence of neighboring trajectories in phase space, i.e., it indicates whether the system is stable, chaotic, or in a state between these modes. Current streamlines and eddy structures are visible in the distribution of the Lyapunov exponent accumulated over the past 15 days (Fig. 3). The black bands in Fig. 3 are often referred to as ridges (Prants et al., 2015). The ridges represent the areas of the flow with the maximum value of the Lyapunov exponent, which indicates the rate of exponential divergence (convergence) of initially close trajectories in a dynamical system and provides information about its long-term behavior and predictability. The distribution of the Lyapunov exponent allows us to identify areas of stability or instability in the system and indicates structures in the form of eddies and ridges that stretch from hyperbolic points (denoted on the L- and S-maps as green crosses). The black ridges on the presented L-maps clearly denote the eddy structures previously identified from SAR images and S-maps Fig. 3.

The L- and S-maps from the GOFS 3.1 reveal vortices as coherent structures with clearly defined borders. On the contrary, the eddies from the GLORYS 12 V1 fields have more sophisticated morphology which complicates the identification of the eddy characteristics. The eddy signatures on the S- and L-maps from GLORYS 12 V1 are closer to the ground truth data in terms of the complexity of the turbulent eddy field in the ROI on chosen dates. On the contrary, the GOFS 3.1 data reproduce more comprehensive and simplified structures which are easier to analyze.

4. Discussion and conclusion

The modeling of the physical processes in the MIZ is a challenging task. In this study, we presented a specific test case on the intercomparison of the eddy fields in the MIZ in the Fram Strait acquired from satellite remote sensing SAR data and complementary data from the Lagrangian modeling based on the two global oceanographic reanalysis GOFS 3.1 and GLORYS 12 V1. Most importantly, this is the first study where such an approach is implemented for the eddy analysis not only in the Fram Strait but for MIZ in the Arctic in general.

The eddy structures identified from the SAR images have corresponding eddy signatures in the S- and L-maps from both GLORYS 12 V1 and GOFS 3.1. There is a significant displacement between the eddy centers identified from the SAR and model data with an average value of 27 km and 25 km for the SAR-GLORYS 12 V1 and SAR-GOFS 3.1 respectively. Nevertheless, both the Lagrangian maps and satellite scenes consistently provide the same result on the rotational direction of the eddy signatures. Based on the information provided by the consequent SAR scenes, we can conclude that the images represent different development stages of the same eddy.

We rely on the accumulation of floating sea ice in the MIZ as the passive tracer which reveals the eddy spiral structures in the surface

Table 1

Characteristics of eddy signatures detected from the SAR and reanalyses data. The scale parameter represents the average of semi-major and semi-minor axes of an eddy elliptical contour. The distance parameter is the distance between eddy centers from the SAR image and reanalyses data.

Date	Source	Lat	Lon	Polarity	Scale [km]	Distance [km]
03.01.2023	SAR	79.85°N	4.0°E	CE	34.55	–
	GLORYS 12 V1	79.9°N	4.0°E	CE	57.75	8.6
	GOFS 3.1	79.9 N	4.0E	CE	49.4	24.4
04.01.2023	SAR	79.7°N	3.1°E	CE	23.75	–
	GLORYS 12 V1	80.0°N	3.9°E	CE	56.3	20.3
	GOFS 3.1	79.76°N	4.65°E	CE	34.5	34.6
08.01.2023	SAR	79.9°N	3.8°E	CE	46.1	–
	GLORYS 12 V1	80.0°N	5.0°E	CE	49.4	24.4
	GOFS 3.1	79.86°N	4.26°E	CE	55.1	14.4
09.01.2023	SAR	79.9°N	3.1°E	CE	34.5	–
	GLORYS 12 V1	79.9°N	5.0°E	CE	55.1	37.5
	GOFS 3.1	79.8°N	4.13°E	CE	36.5	23.1
10.01.2023	SAR	79.8 N	3.1E	CE	36.5	–
	GLORYS 12 V1	80.0°N	4.4°E	CE	46.35	43.9
	GOFS 3.1	79.77°N	4.15°E	CE	46.35	31.2
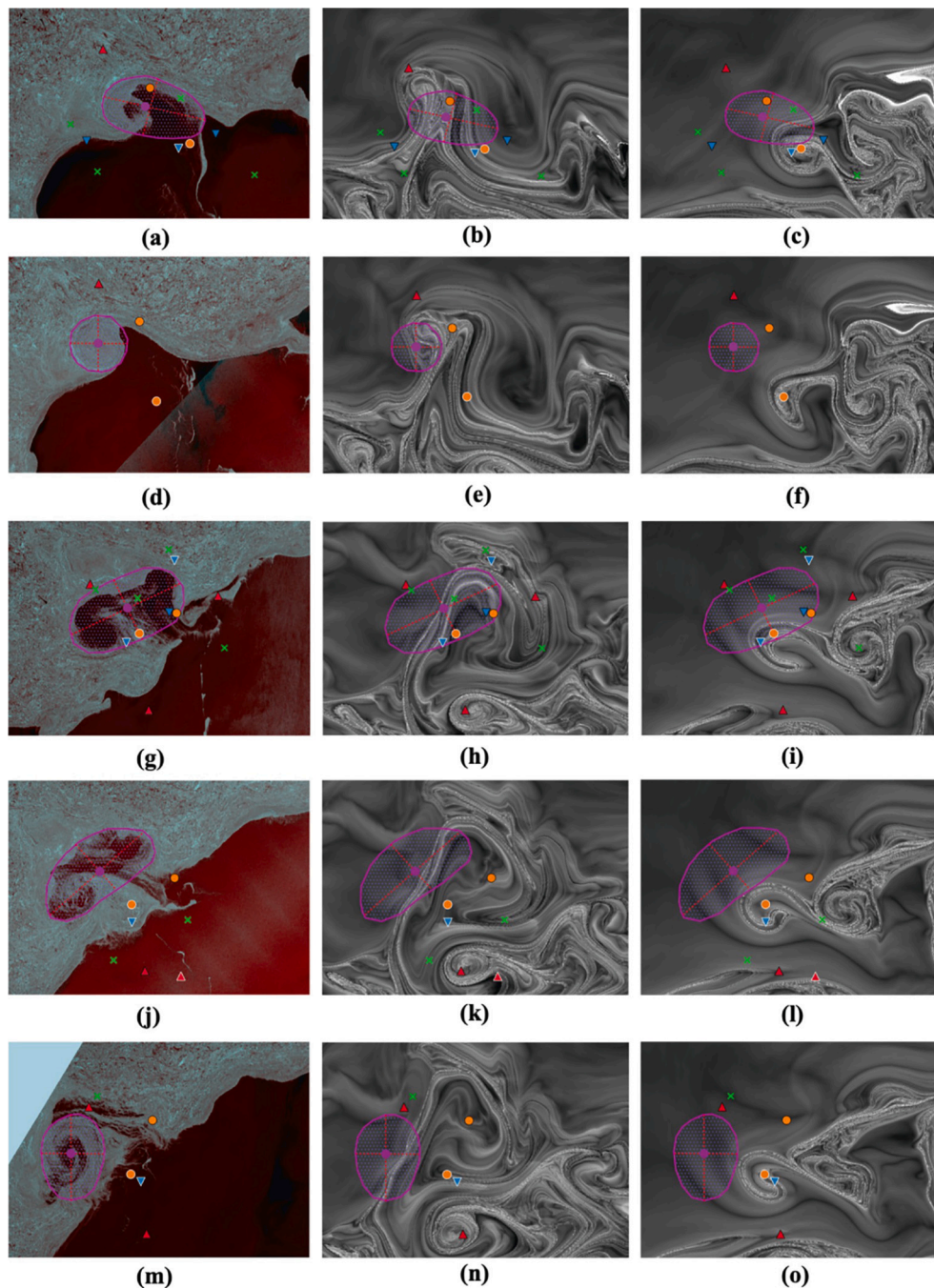
Fig. 3. False-color composite representations of Sentinel-1 SAR images (first column), L-maps obtained from the GLORYS 12 V1 (second column), and GOFS 3.1 (third column) for 3 (a–c), 4 (d–f), 8 (g–i), 9 (j–l), and 10 (m–o) of January 2023. The description of the cartographic symbols can be found in the caption of Fig. 2.

layer on the SAR images. The sea ice in the MIZ is susceptible to the influence of wind, which is not taken into account in comparison to the SAR and model data. Hence, the bias in eddy locations from SAR and model data could be partially explained by the influence of the wind forcing on the ice field leading to the additional ice drift.

Despite the difference in the spatial scales and location of eddy centers, the agreement in the eddy polarity and synchronism with reality is encouraging and supports the further use of the presented approach for studying the eddies in the MIZ regions in the Arctic. Due to the limited sampling, we are not in a position to make far-reaching conclusions. However, based on the obtained results it seems that data from the GOFS 3.1 reanalysis could be more promising for studying the eddy variability in the MIZ due to the more simplistic representation of the

eddy field, which makes it easier to define characteristics of single eddies. Nevertheless, both reanalyses can be used as a complementary source for eddy detection in the MIZ. Accordingly, it is of crucial importance to dig deeper into this topic to obtain more results on this matter.

It should be also taken into consideration that the accuracy of the eddy identification in MIZ can be significantly affected by the individual eddy characteristics, such as size. Moreover, the representation of eddy dynamics in the MIZ is strongly connected to SIC (Kozlov et al., 2019b). The general presence or absence of sea ice, shape and smoothness of the sea ice edge differ for both reanalyses. Hence, one of the potential further directions that can improve our understanding of the eddy variability in the MIZ is to obtain significantly long data series on

physical and geometrical eddy properties from both modeling or reanalyses and SAR data. Moreover, that will allow us to conduct a comparison study of eddy census statistics between these two complementary sources. This approach involves the implementation of the automatic eddy detection algorithms to both SAR and model/reanalysis data in the MIZ. The first steps towards the automatization of eddy detection in the MIZ were already done in the study by Khachatrian et al. (Khachatrian et al., 2023).

CRediT authorship contribution statement

Nikita Sandalyuk: Writing – review & editing, Writing – original draft, Visualization, Methodology, Formal analysis, Data curation, Conceptualization. **Eduard Khachatrian:** Writing – review & editing, Writing – original draft, Visualization, Methodology, Formal analysis, Data curation, Conceptualization. **Maxim Budyansky:** Writing – review & editing, Writing – original draft, Methodology, Data curation.

Declaration of competing interest

The authors declare that they have no known competing financial interests or personal relationships that could have appeared to influence the work reported in this paper.

Data availability

Data will be made available on request.

References

Bashmachnikov, I., Kozlov, I., Petrenko, L., Glock, N., Wekerle, C., 2020. Eddies in the North Greenland Sea and fram strait from satellite altimetry, Sar and high-resolution model data. J. Geophys. Res. Oceans. https://doi.org/10.1029/2019JC015832, 07.

Budyansky, M., Prants, S., Uleysky, M., 2022. Odyssey of aleutian eddies. Ocean Dyn. 72, 455–476. https://doi.org/10.1007/s10236-022-01508-w.

Chelton, D.B., Schlax, M.G., Samelson, R.M., 2011. Global observations of nonlinear mesoscale eddies. Prog. Oceanogr. 91 (2), 167–216. https://doi.org/10.1016/j.pocean.2011.01.002. URL. https://www.sciencedirect.com/science/article/pii/S0079661111000036.

Faghmous, J., Frenger, I., Yao, Y., Warmka, R., Lindell, A., Kumar, V., 2015. A daily global mesoscale ocean eddy dataset from satellite altimetry. Scientific Data 2, 150028. https://doi.org/10.1038/sdata.2015.28.

Jayne, S.R., Marotzke, J., 2002. The oceanic eddy heat transport. J. Phys. Oceanogr. 32 (12), 3328–3345. https://doi.org/10.1175/1520-0485(2002)032<3328:TOEHT>2.0.CO;2. URL. https://journals.ametsoc.org/view/journals/phoc/32/12/1520-0485_2002_032_3328_toeht_2.0.co_2.xml.

Jean-Michel, L., Eric, G., Romain, B.-B., Gilles, G., Angélique, M., Marie, D., Clément, B., Mathieu, H., Olivier, L.G., Charly, R., Tony, C., Charles-Emmanuel, T., Florent, G., Giovanni, R., Mounir, B., Yann, D., Pierre-Yves, L.T., 2021. The copernicus global 1/12° oceanic and sea ice glorys12 reanalysis. Front. Earth Sci. 9 https://doi.org/10.3389/feart.2021.698876. URL. https://www.frontiersin.org/articles/10.3389/feart.2021.698876.

Johannessen, J.A., Johannessen, O.M., Svendsen, E., Shuchman, R., Manley, T., Campbell, W.J., Josberger, E.G., Sandven, S., Gascard, J.C., Olaussen, T., Davidson, K., Van Leer, J., 1987. Mesoscale eddies in the fram strait marginal ice zone during the 1983 and 1984 marginal ice zone experiments. J. Geophys. Res. Oceans 92 (C7), 6754–6772. arXiv. https://agupubs.onlinelibrary.wiley.com/doi/pdf/10.1029/JC092iC07p06754. https://doi.org/10.1029/JC092iC07p06754. URL. https://agupubs.onlinelibrary.wiley.com/doi/abs/10.1029/JC092iC07p06754.

Khachatrian, E., Sandalyuk, N., Lozou, P., 2023. Eddy detection in the marginal ice zone with sentinel-1 data using yolov5. Remote Sens. 15 (9) https://doi.org/10.3390/rs15092244. URL. https://www.mdpi.com/2072-4292/15/9/2244.

Kozlov, I.E., Atadzhanova, O.A., 2022. Eddies in the marginal ice zone of fram strait and svalbard from spaceborne Sar observations in winter. Remote Sens. 14 (1). URL. https://www.mdpi.com/2072-4292/14/1/134.

Kozlov, I., Kozlov, I., Petrenko, L.A., Plotnikov, E., Plotnikov, E., 2019a. Statistical and dynamical properties of ocean eddies in fram strait from spaceborne Sar observations. Remote Sens. https://doi.org/10.1117/12.2533317.

Kozlov, I.E., Artamonova, A.V., Manucharyan, G.E., Kubryakov, A.A., 2019b. Eddies in the western arctic ocean from spaceborne Sar observations over open ocean and marginal ice zones. J. Geophys. Res. Oceans 124 (9), 6601–6616. arXiv. https://agupubs.onlinelibrary.wiley.com/doi/pdf/10.1029/2019JC015113. https://doi.org/10.1029/2019JC015113. https://agupubs.onlinelibrary.wiley.com/doi/abs/10.1029/2019JC015113.

Kozlov, I.E., Plotnikov, E.V., Manucharyan, G.E., 2020. Brief communication: mesoscale and submesoscale dynamics in the marginal ice zone from sequential synthetic aperture radar observations. Cryosphere 14 (9), 2941–2947. https://doi.org/10.5194/tc-14-2941-2020. URL. https://tc.copernicus.org/articles/14/2941/2020/.

Ma, W., Xiu, P., Chai, F., Ran, L., Wiesner, M.G., Xi, J., Yan, Y., Fredj, E., 2021. Impact of mesoscale eddies on the source funnel of sediment trap measurements in the South China Sea. Prog. Oceanogr. 194, 102566. https://doi.org/10.1016/j.pocean.2021.102566. URL. https://www.sciencedirect.com/science/article/pii/S0079661121000537.

Madec, G., 2008. Nemo Ocean engine, project report. URL. https://eprints.soton.ac.uk/64324/.

Mason, E., Pascual, A., McWilliams, J.C., 2014. A new sea surface height–based code for oceanic mesoscale eddy tracking. J. Atmos. Ocean. Technol. 31 (5), 1181–1188. https://doi.org/10.1175/JTECH-D-14-00019.1. URL. https://journals.ametsoc.org/view/journals/atot/31/5/jtech-d-14-00019_1.xml.

Pegliasco, C., Delepoulle, A., Mason, E., Morrow, R., Faugère, Y., Dibarboure, G., 2022. Meta3.1exp: a new global mesoscale eddy trajectory atlas derived from altimetry. Earth System Science Data 14 (3), 1087–1107. https://doi.org/10.5194/essd-14-1087-2022. URL. https://essd.copernicus.org/articles/14/1087/2022/.

Prants, S., Budyansky, M., Ponomarev, V., Uleysky, M., 2011. Lagrangian study of transport and mixing in a mesoscale eddy street. Ocean Model 38 (1), 114–125. https://doi.org/10.1016/j.ocemod.2011.02.008. URL. https://www.sciencedirect.com/science/article/pii/S1463500311000436.

Prants, S., Andreev, A., Budyansky, M., Uleysky, M., 2013. Impact of mesoscale eddies on surface flow between the pacific ocean and the bering sea across the near strait. Ocean Model 72, 143–152. https://doi.org/10.1016/j.ocemod.2013.09.003. URL. https://www.sciencedirect.com/science/article/pii/S1463500313001650.

Prants, S., Budyansky, M., Uleysky, M., Zhang, J., 2015. Hyperbolicity in the ocean. Discontinuity, Nonlinearity, and Complexity 12 (3), 257–270. https://doi.org/10.5890/DNC.2015.09.004.

Prants, S., Lobanov, V., Budyansky, M., Uleysky, M., 2016. Lagrangian analysis of formation, structure, evolution and splitting of anticyclonic kuril eddies. Deep-Sea Res. I Oceanogr. Res. Pap. 109, 61–75. https://doi.org/10.1016/j.dsr.2016.01.003. URL. https://www.sciencedirect.com/science/article/pii/S0967063715300546.

Prants, S., Uleysky, M., Budyansky, M., 2017. Lagrangian oceanography. Springer Cham, Berlin, N. Y.. https://doi.org/10.1007/978-3-319-53022-2

Prants, S., Budyansky, M., Fayman, P., et al., 2023. Lagrangian oil spill simulation in peter the great bay (sea of Japan) with a high-resolution roms model. Pure Appl. Geophys. 180, 551–568. https://doi.org/10.1007/s00024-022-03197-4.

Roscher, R., Uebbing, B., Kusche, J., 2017. Star: Spatio-temporal altimeter waveform retracking using sparse representation and conditional random fields. Remote Sens. Environ. 201, 148–164. https://doi.org/10.1016/j.rse.2017.07.024. URL. https://www.sciencedirect.com/science/article/pii/S0034425717303395.

Sandven, S., Johannessen, O.M., Kloster, K., 1993. Sea ice monitoring by remote sensing, encyclopedia of. Anal. Chem. March 1993 (2006), 1–43. https://doi.org/10.1002/9780470027318.a2320.

Shinoda, T., Tissot, P., Reisinger, A., 2023. Influence of loop current and eddy shedding on subseasonal sea level variability along the western gulf coast. Front. Mar. Sci. 9 https://doi.org/10.3389/fmars.2022.1049550. URL. https://www.frontiersin.org/articles/10.3389/fmars.2022.1049550.

Travkin, V.S., Belonenko, T.V., Budyansky, M.V., et al., 2022. Quasi-permanent mushroom-like dipole in the lofoten basin. Pure Appl. Geophys. 179, 465–482. https://doi.org/10.1007/s00024-021-02922-9.

Verezemskaya, P., Barnier, B., Gulev, S.K., Gladyshev, S., Molines, J.-M., Gladyshev, V., Lellouche, J.-M., Gavrikov, A., 2021. Assessing eddying (1/12°) ocean reanalysis glorys12 using the 14-yr instrumental record from 59.5°n section in the atlantic. J. Geophys. Res. Oceans 126 (6) e2020JC016317, e2020JC016317 2020JC016317. arXiv. https://agupubs.onlinelibrary.wiley.com/doi/pdf/10.1029/2020JC016317. https://doi.org/10.1029/2020JC016317. URL. https://agupubs.onlinelibrary.wiley.com/doi/abs/10.1029/2020JC016317.

von Appen, W.-J., Schauer, U., Somavilla, R., Bauerfeind, E., Beszczynska-Möller, A., 2015. Exchange of warming deep waters across fram strait. Deep-Sea Res. I Oceanogr. Res. Pap. 103, 86–100. https://doi.org/10.1016/j.dsr.2015.06.003. URL. https://www.sciencedirect.com/science/article/pii/S0967063715001077.

von Appen, W.-J., Schauer, U., Hattermann, T., Beszczynska-Möller, A., 2016. Seasonal cycle of mesoscale instability of the west spitsbergen current. J. Phys. Oceanogr. 46 (4), 1231–1254. https://doi.org/10.1175/JPO-D-15-0184.1. URL. https://journals.ametsoc.org/view/journals/phoc/46/4/jpo-d-15-0184.1.xml.

von Appen, W.-J., Wekerle, C., Hehemann, L., Schourup-Kristensen, V., Konrad, C., Iversen, M.H., 2018. Observations of a submesoscale cyclonic filament in the marginal ice zone. Geophys. Res. Lett. 45 (12), 6141–6149. arXiv. https://agupubs.onlinelibrary.wiley.

com/doi/pdf/10.1029/2018GL077897. https://doi.org/10.1029/201
8GL077897. URL. https://agupubs.onlinelibrary.wiley.
com/doi/abs/10.1029/2018GL077897.

Wallcraft, A., Metzger, E., Carroll, S., 2009. Software design description for the hybrid
coordinate ocean model (hycom), version 2.2, 02.

Wang, X., Ichikawa, K., 2017. Coastal waveform retracking for jason-2 altimeter data
based on along-track echograms around the Tsushima islands in Japan. Remote Sens.
9 (7) https://doi.org/10.3390/rs9070762. URL. https://www.mdpi.
com/2072-4292/9/7/762.

Q. Wang, N. V. Koldunov, S. Danilov, D. Sidorenko, C. Wekerle, P. Scholz, I. L.
Bashmachnikov, T. Jung, Eddy kinetic energy in the arctic ocean from a global
simulation with a 1-km arctic, Geophys. Res. Lett. 47 (14) (2020) e2020GL088550,
e2020GL088550 https://doi.org/10.1029/2020GL088550. arXiv:
https://agupubs.onlinelibrary.wiley.
com/doi/pdf/10.1029/2020GL088550, doi:https://doi.org/10.1029/202
0GL088550. URL https://agupubs.onlinelibrary.wiley.
com/doi/abs/10.1029/2020GL088550.

Wekerle, C., Hattermann, T., Wang, Q., Crews, L., von Appen, W.-J., Danilov, S., 2020.
Properties and dynamics of mesoscale eddies in fram strait from a comparison
between two high-resolution ocean–sea ice models. Ocean Sci. 16 (5), 1225–1246.
https://doi.org/10.5194/os-16-1225-2020. URL. https://os.copernicus.
org/articles/16/1225/2020/.

WMO, 1970. WMO Sea-ice Nomenclature: Terminology, Codes, Illustrated Glossary and
Symbols, no. 4 in WMO sea-ice nomenclature, Secretariat of the World
Meteorological Organization. URL. https://books.google.rs/books?
id=BRVUmwEACAAJ.

Zhang, Y., Chambers, D., Liang, X., 2021. Regional trends in southern ocean eddy kinetic
energy. J. Geophys. Res. Oceans 126 (6) e2020JC016973, e2020JC016973
2020JC016973. arXiv. https://agupubs.onlinelibrary.wiley.
com/doi/pdf/10.1029/2020JC016973. https://doi.org/10.1029/2020JC01
6973. URL. https://agupubs.onlinelibrary.wiley.
com/doi/abs/10.1029/2020JC016973.